Evidence of dispersion and refraction of a spectrally broad gravity wave packet in the mesopause region observed by the Na lidar and Mesospheric Temperature Mapper above Logan, Utah

Yuan T[1], C. J. Heale[3], J. B. Snively[3], X. Cai[1,2], P.-D. Pautet[1], C. Fish[4], Y. Zhao[1], M. J. Taylor[1, 2], W. R. Pendleton, Jr[1], V. Wickwar[1,2], N. J. Mitchell[5]

1. Center for Atmospheric and Space Sciences, Utah State University
2. Physics Department, Utah State University
3. Embry-Riddle Aeronautical University
4. Space Dynamic Laboratory, Utah State University
5. Department of Electronic & Electrical Engineering, University of Bath

Corresponding author: Tao Yuan

Email: titus.yuan@usu.edu

This article has been accepted for publication and undergone full peer review but has not been through the copyediting, typesetting, pagination and proofreading process which may lead to differences between this version and the Version of Record. Please cite this article as doi: 10.1002/2015JD023685

Abstract:

Gravity wave packets excited by a source of finite duration and size possess a broad frequency and wavenumber spectrum, and thus span a range of temporal and spatial scales. Observing at a single location relatively close to the source, the wave components with higher frequency and larger vertical wavelength dominate at earlier times and at higher altitudes while the lower frequency components, with shorter vertical wavelength, dominate during the latter part of the propagation. Utilizing observations from the Na lidar at Utah State University and the nearby Mesospheric Temperature Mapper (MTM) at Bear Lake Observatory (BLO) [41.9°N, 111.4°W], we investigate a unique case of vertical dispersion for a spectrally broad gravity wave packet in the mesopause region over Logan, Utah (41.7°N, 111.8°W) that occurred on September 2nd, 2011, to study the waves' evolution as it propagates upward. The lidar observed temperature perturbation was dominated by close to a 1-hour modulation at 100 km during the early hours, but gradually evolved into a 1.5-hour modulation during the second half of the night. The vertical wavelength also decreased simultaneously, while the vertical group and phase velocities of the packet apparently slowed, as it was approaching a critical level during the second half of the night. A two-dimensional numerical model is used to simulate the observed GW processes, finding that the location of the lidar relative to the source can strongly influence which portion of the spectrum can be observed at a particular location relative to a source.

Key points:

1. **Evidence of dispersion for a spectrally broad gravity wave in mesopause region**
2. **Collaborative Na lidar and mesospheric temperature mapper observations**
3. **Numerical model simulation of the gravity wave propagation and dispersion**

Introduction:

Gravity waves (GW) can be generated through convection, wind shear, topography and other sources at lower altitudes [Fritts and Alexander, 2003]. GW packets propagate away from their sources and experience dissipation via viscosity, wind filtering, or nonlinear breaking and instability. Such dissipation processes are critical for upper atmospheric dynamics and chemistry, since these mechanisms transfer and deposit the energy and momentum that the waves inherit from their sources while affecting the dynamic flow and thermal structures in the mesosphere and lower thermosphere. Fritts and Alexander [2003] reviewed these processes including GW propagation, dissipation and its associated instabilities, turbulent mixing, momentum etc. Later, Alexander and Holton [2004] found that GW packets generated by transient tropospheric convection, such as that associated with cumulus clouds, have quite broad frequency spectra and a wide range of vertical scales. They also pointed out that the GW characteristics observed by ground-based observatories can be very sensitive to the distance relative to the source and the observation (including both horizontal and altitude ranges). The results suggest that at a certain altitude in the upper atmosphere, the high frequency, long vertical wavelength components, which are believed to account for a significant share of gravity wave momentum flux in the mesosphere [e.g., Fritts et al., 2014a], are primarily observed at close range relative to the source except in cases of reflection and ducting [e.g., Walterscheid et al., 2001; Heale et al., 2014b], while the low frequency components arrive later due to slower vertical wave speed.

In the mesopause region where the dissipation by molecular viscosity is not dominant, such transitions from high frequency to low frequency are not expected to be easily detected even at a station that close to the source. This is because the amplitudes of components within a GW packet's continuous spectrum vary dramatically over a wide

altitude range. The highest vertical phase velocity components often have relatively small amplitudes as compared to the dominant components of the packet that may be observed as they pass through the mesopause region. The fastest waves become significant and measurable only when they propagate well into the thermosphere, while MLT region observations appear more likely to reveal dispersion of the small-to-medium scale waves with intermediate group velocities ~10-100 m/s, e.g., Heale et al., (2014a). Various model and numerical simulation works [Fritts and Vadas, 2008; Yu et al., 2009; Liu et al., 2013; Heale et al., 2014a] have been conducted to investigate the GW packet propagation, dispersion and dissipation in the upper atmosphere. When studying the GW packet behaviors in the lower thermosphere, Heale et al. [2014a] found the reduction of the vertical wavelength in time due to effect of dispersion and subsequent damping of waves by molecular viscosity in the thermosphere, which is in agreement with earlier model studies [Vadas and Fritts, 2005; Liu et al., 2013]. During the time evolution of a spectrally broad GW packet, the simulation shows that the high frequency components with long vertical wavelength also have large vertical group velocities and thus reach the highest altitudes and dissipate first. This leaves the slower, low frequency components with shorter vertical wavelength to reach high altitudes and become dominant at later times. The transition from the long vertical wavelength to shorter one can be clearly seen in Fig. 4b of Heale et al., [2014a], which shows the evolution of the horizontal wind with time. Although we note this study was conducted in a periodic domain, so there is technically no distance from the source in the horizontal direction, the same dispersive separation can be expected for packets that are compact in the horizontal direction. Indeed, the group velocities of waves within a spectrum determine the spatial evolution of the packet's extent over time.

In parallel to these modeling studies, extensive ground-based observational studies have been conducted for GW dynamics in the Mesosphere Lower Thermosphere (MLT)

region, although most analyses focus on quasi monochromatic events [Cai et al., 2014; Li et al., 2007a; Li et al., 2007b; Lu et al., 2009 and Chen et al., 2013]. On the other hand, little empirical evidence has been reported to confirm the key phenomenon described by the above simulated GW packet propagation, dispersion, and dissipation process, in which the apparent dominant wave signature evolves from high frequency components most-detectable at high altitudes to ones with lower frequency at later time and lower altitudes with its vertical wavelength decreasing simultaneously, leaving the dispersive evolution of gravity waves mostly unnoticed. This is partly due to the fact that, at single location, observing a narrow altitude range of the upper atmosphere, only a portion of the entire GW spectrum may be present and observable. At large distances away from the sources, most of the observable dominant waves are typically high frequency and nearly ducted, e.g., Snively et al., [2013] and Heale et al. [2014b], or belong to the low frequency and short vertical wavelength section of the whole spectrum, while other parts of the GW packet components may have already dissipated, been filtered or passed through the observing altitude range at a different horizontal position to where the measurements are made.

In this paper, we study one unique event that the Na lidar at Utah State University (USU) captured on September 2nd, 2011, which closely resembles the above mentioned model results of a spectrally broad GW packet as it propagates and disperses. Utilizing USU's suite of nearby instruments at Bear Lake Observatory (BLO), including a Mesospheric Temperature Mapper (MTM) and Meteor Wind Radar (MWR), we conduct comprehensive diagnosis of this event. A fully compressible, nonlinear 2-D numerical model [Snively and Pasko, 2008; Snively, 2013; Heale at al., 2014a] is also utilized to simulate this event, by constraining the conditions of the model run using these observations results, including GW packet parameters, temperature and horizontal wind background. The paper is laid out as follows: the instruments involved are briefly described in Section 2; experimental

observations and measurements of the event are discussed in Section 3; the model simulation and associated discussion are presented in Section 4; conclusions are articulated in Section 5.

2. Instruments

The Na lidar facility, complemented by the MTM and MWR at BLO located ~ 40 km northeast of Logan, is an advanced resonance fluorescence Doppler lidar system operating at the Na D_{2a} line (589.158 nm) with a 120MHz FWHM (Full Width Half Maximum) laser pulse bandwidth. Utilizing the naturally existing Na layer in the upper atmosphere, it can provide critical atmospheric information, such as neutral temperature, and horizontal wind along with Na density profiles throughout a full diurnal cycle of observations of the mesopause region (80-110 km) [She et al., 2003; 2004]. For gravity wave and small scale dynamics studies, the lidar data can be processed with high resolutions. One of the advantages of this advanced lidar system is that the tidal period perturbations can also be removed to avoid bias in estimations of mean fields and gravity wave parameters [Cai et al., 2014; Yuan et al., 2014]. For the investigation of this event, a 1-km FWHM Hanning sliding window is applied in the vertical direction and 10-minute integration times are utilized to bin the lidar data. On the night of September 2nd, 2011, the Na lidar was pointing one of its beams in the zenith direction and using one 1.25-meter diameter mirror of the USU Rayleigh lidar receiver to collect the return photo echoes to boost the signal to noise ratio. During the same night, the meridional wind was measured from the north pointing lidar beam (30 degree off zenith) coupled with a 0.3 m diameter Celestron-14 telescope. In this paper, we set the upper limit of the temperature uncertainty at 15 K to reject inferior measurements.

At the nearby BLO, the University of Bath SkiYMet MWR provided continuous horizontal wind measurements. The MWR is an all-sky interferometric system [Hocking et al., 2001] that employs a high pulse repetition sounding to detect and measure meteor trail

echoes. The MWR transmits continuously at a fixed frequency of 32.5 MHz, with a power output of ~ 6 kW using a crossed Yagi antenna, and receives on a 5-Yagi (crossed) antenna configuration. Each hour, a horizontal wind vector is fitted to 3-km wide height bins over a sampled height interval of 83–98 km. The MWR meteor trails are detected primarily at mid to low-elevation angles and represent an average wind over a horizontal region of ~ 400 km in diameter, centered on BLO. The standard uncertainty for MWR horizontal wind measurement is ~ ± 5 m/s.

The mesospheric temperature mapper (MTM) is a CCD-based instrument developed at Utah State University. It is installed and operating at BLO alongside the MWR. It images a ~ 90° (field of view) area of the sky, centered on the zenith, using a back-illuminated 1024x1024 pixels CCD detector (binned down to 128x128 pixels to improve the signal-to-noise ratio), a telecentric lens system and 3 narrow-band filters to sequentially measure the P1(2) and P1(4) lines of the OH (6,2) Meinel band and the sky background intensity at 857nm (Pendleton et al., 2000; Taylor et al., 2001). In 2001, this instrument was improved to include measurements of the intensity of 2 well-defined regions of the O_2 (0,1) atmospheric band at 866 and 868nm. This emission is located slightly higher (~ 94km) than OH, adding complementary altitude information on the atmospheric temperature. The exposure time for each line is typically 60s, which gives two temperature measurements at two different altitudes (87 and 94km) every ~ 5.5 minutes. Rotational temperatures can be computed separately for the OH and the O_2 emissions using the well-established 'ratio method', as described by Meriwether (1984).

3. Observations

Figure 1 shows the Na density and temperature observations by the USU Na lidar on the night of September 2nd, 2011 (245th day of the year) from the zenith pointing lidar beam,

labeled as “sg2”. From the figure, the strong GW modulations can be easily seen in both lidar measurements, but more pronounced (in part due to scaling) in the temperature observations. During the first half of the night, the modulation of the temperature at higher altitudes is close to 20 K peak-to-peak. The first half of the night was dominated by the modulation with long vertical wavelength, but changed to the component with shorter vertical wavelength during the second half of the night within the bottom half of mesopause region. Such gradual variation of the vertical wavelength can also be observed in the Na density variation. The perturbations’ downward phase progression suggests that this is part of an upward propagating GW packet. The modulation above 94 km disappeared after 09:00 UT, and it was limited below 92 km by the end of the night. From the figure, the period of the modulation at higher altitudes also appeared to be shorter than that of the lower altitudes. This data set is unique, in that while most of the reported GW event studies from the ground-based instruments report quasi-monochromatic events or series of a few clearly discrete GW oscillations, this event appears as a gradual and smooth variation of GW parameters over time. This seems to be associated with the propagation of a single GW packet at medium scale with a relatively broad (and dispersed) temporal spectrum, which is unusual in the context of previously reported wave events.

To quantitatively investigate the frequency spectrum variations throughout the night, the Morlet wavelet analysis [Press et al. 1992] is performed at 85 km, 87 km, 94 km and 100 km on temperature perturbations, as shown in Figure 2. The wavelet results at 87 km and 94 km are chosen to compare with MTM measurements at OH and O_2 level. Although the wavelet analysis sacrifices some spectral resolution, it can resolve the spectra of each wave-packet as functions of time for each altitude. Here, the temperature data are band-pass filtered to retain perturbations with periods between 50-minutes and 3-hours. Thus, components with period outside the bandwidth of the filter are not expected in the figure. Figure 2a-2d shows the

wavelet results at these four altitudes: at 85 km, starting from 06:00 UT, the dominant component had a period of slightly above 1.5-hours (90-minutes) for most of the night; at 100 km, the first component appeared between ~04:00 UT and ~06:30 UT with a period centered at roughly 1.2-hours, thereafter, it switched to some weak component with much longer period of ~2.5-hours and there was not much strong modulation for the rest of the night at this altitude. This is most likely due to horizontal wind filtering effect that is explained in the later part of this section; similar to the scenario at 100 km, near the O_2 layer (94 km), the spectrum was mixed with a period between 1 hours to 1.5-hours before 08:00 UT but followed by weak modulation with a period longer than 2-hours; slightly below, within the OH layer (87 km) altitude, the spectrum seems to be opposite to that of O_2 altitude, mixed with a longer period (~1.3-hours to ~2-hours) during the first half of the night, but a shorter period (~1.1-hours to ~1.3-hours) in the second half. It is worth noting there was a similar transition at 94 km around 07:00 UT, but in much less time scale. This effect could be due to wave breaking in the lidar data at later time, which causes the formation of smaller scale and shorter period structures. In addition, ray-trace theory suggests that a changing background wind can modulate the ground relative frequency of a GW, i.e. $\frac{d\omega}{dt} = \omega\frac{dU}{dt}$. It could be that the phase and timing of the background wind at 87km is such that it increases the frequency of the gravity wave as it propagates through this region, thus leading to a transition from longer to shorter periods. Indeed, at later times at 87 km (around 8-9 UT), the wind turns northward and dU/dt is maximized (see Figure 8b). Over all, based on these lidar results, the shifting from high frequency modulations at higher altitudes to low frequency ones below 90 km is evident, with additional complexity detected at the altitudes of the OH layer.

During the same night, the USU MTM installed at nearby BLO observed a similar variation of period between the O_2 (~94 km ± 3 km) and OH (~87 km ± 5 km) layers. Figure 3 shows the East-West and North-West sliced Keograms of the rotational temperatures from

the O_2 and OH channels. The data are filtered to focus on GW modulations with periods between 60 and 120 minutes, and the periods of this large scale waves are deduced using FFT processing [Fritts et al., 2014a]. From the figure, it is apparent that the modulation near 94 km had higher frequency than that near 87 km. Indeed, near the O_2 layer, the MTM data indicate a modulation mostly near 1.25 hour, while the data from the OH layer shows an averaged observed period of 1.5-hour. Also, the modulations during the first half of the night were much stronger than those in the second half of the night, which also agrees with the lidar observations. The large values of temperatures in O_2 signal near 12:00 UT are mostly due to saturation from the sunlight during the early morning. The horizontal wavelengths at these two levels are measured to be ~ 290 km and ~ 260 km with observed horizontal phase speeds of ~ 64 m/s and ~ 46 m/s, respectively. The packet was also found to be traveling ~ 355° relative to the north that night. However, it has to be pointed out here that the uncertainties of the measured horizontal wavelength and phase speeds for such large scale waves by MTM are relatively larger (~10%) than those of the measured small scale waves (~1%) due to the instrument's limited field of view. It is also important to note that the MTM results are the "average" through the whole OH or O_2 layer. Thus, some differences are expected between Na lidar and MTM observations.

To quantify the GW packet's parameters, such as intrinsic frequency and vertical wavenumber, horizontal wind information is essential, and the MWR at BLO provided the wind measurements throughout this event. Based on the GW dispersion relationship [Fritts and Alexander, 2003], the GW vertical wavenumber, *m*, can be calculated as

$$m^2 = k^2(N^2/\omega_i^2 - 1) - 1/4H^2 \qquad (1)$$

, where $\omega_i = kc_i = k(c - U_h)$, c and U_h are the GW observed horizontal phase velocity by MTM and the mean wind in the direction of GW propagation measured by MWR, $c_i = k(c - U_h)$ is

the GW intrinsic phase speed, *k* represents the observed horizontal wavenumber. Since the packet was propagating almost strictly to the north that night (355° relative to the north), U_h is very close to meridional wind, which will represent U_h for the reminder of the paper. The buoyancy frequency, *N*, and scale height, *H*, are both calculated based upon the Na lidar background temperature observations, T_0. Here, the lidar data at each altitude are further processed with a Butterworth filter that removes perturbations with period less than 30 minutes. Then, the time series of background temperatures for each altitude, T_0, are deduced from a 2-hour window, sliding across this new set of lidar temperature data at 10-minute step. The time series of the temperature variances (discussed later), T'^2, at each altitude for the later discussed GW momentum flux calculations are also derived in the same process. However, due to the width of the 2-hour sliding window, this approach cannot calculate the momentum flux near the beginning and end of the lidar observation. Thus, we utilize T'^2 *deduced* from the first and last window, along with T_0 deduced from a 2-hour boxcar averaged for the momentum flux calculation on both ends of the lidar observation.

Furthermore, we can evaluate the GW vertical group velocity, V_{gz}, near the two nightglow layers, by using

$$V_{gz} = \frac{-m\omega_i^2}{\omega_i(k^2+m^2+1/4H^2)} \qquad (2)$$

, based on the Hines inviscid relation (1960). The vertical wavenumber, *m,* should be negative in this case, representing upward wave propagation or downward phase progression.

Figure 4a and 4b show the calculated variations of vertical wavelength and GW vertical group velocities near the two nightglow levels. It is evident that, near both altitudes, the GW packet vertical wavelength were decreasing during the night, from around 40 km near the beginning of the night to close to zero in the early morning. The gradual decrease of

vertical wavelength occurring near both the O_2 and OH levels is most likely due both to the dispersion of the spectrum as it propagates and to the packet approaching a critical level near this height as the wind flow evolves. During the same time, the vertical group velocity of the packet was slowing down, from ~10 m/s near OH level and ~15 m/s near O_2 level, to close to zero by the end of the night. It is worth noting that the GW packet reached zero speed earlier (07:30 UT) near O_2 layer than it did near OH layer (near 09:30 UT). This could be caused by the increasing of northward horizontal wind in the GW's horizontal propagating direction that generated critical levels for this packet. Indeed, the lidar meridional wind measurement shows the critical level was likely formed around UT 08:30 near the O_2 level, while that near OH level was formed at later time around UT 10:00. Such northward wind enhancement is most likely due to the approaching of the meridional wind semidiurnal tidal maximum during the second half the night [Yuan et al., 2008], which arrives earlier near 94 km than it does near 87 km due to downward tidal wave phase progression.

The gravity wave momentum flux (MF) and its divergence can provide insight into the wave's amplitude and impacts in the mesopause region. In addition to the co-planar lidar beam measurement [Acott et al., 2011], as discussed by Ern et al., (2004) and Alexander et al., (2008), the relation between absolute MF and temperature variance is

$$|u'w'| = \frac{1}{2}\frac{\lambda_z}{\lambda_h}\frac{g^2}{N^2}\frac{T'^2}{T_0^2} = \frac{1}{2}\frac{k}{m}\frac{g^2}{N^2}\frac{T'^2}{T_0^2} \qquad (3)$$

, where λ_z and λ_h are the GW vertical and horizontal wavelength, respectively. Using a similar approach, the most recent work by Fritts et al., (2014a) took advantage of the precise temperature perturbation measurement by an Advanced Mesospheric Temperature Mapper (AMTM) [Pautet et al., 2014], coupled with Na lidar and MWR observations, to estimate GW momentum flux for small scale waves in the mesopause region. Thus, based upon the above

observed parameters of this GW packet and Eq. 3, we can estimate the momentum flux variation during this critical phase of the wave propagation by utilizing the MTM's observations and Na lidar temperature measurements discussed earlier. If we ignore the uncertainties in the MTM observations of horizontal wavelength and phase speeds (relatively small compared to the waves' large horizontal scale, for example, the uncertainty of horizontal wavelength is estimated to be ~ 10% compared to λ_z ~ 260 km near OH layer), the uncertainties of this calculation are dominated by photon noise of the lidar data and the uncertainty in MWR's wind measurement.

Figure 4c shows the calculated MFs near the two nightglow emission levels. Both have very similar variation over the course of the night and exhibit similar magnitudes within the error bars. It also clearly indicates that, although inheriting relatively larger error, the MF in the mesopause region was considerably larger during the first half of the night. Specifically, near both altitudes (87 km and 94 km) the MF started to increase after 04:00 UT and peaked around 05:30 UT ~ 12 m^2/s^2. It was then decreasing until 07:30 UT and staying around 1 m^2/s^2 after 08:30 UT till the end of the night. In other words, the MF was much more significant during the first half of the night when components with long vertical wavelength were dominating the mesopause region. This is in good agreement with the theoretical statements [Fritts and Alexander, 2003; Alexander and Holton, 2004; Vadas and Fritts, 2005; Fritts et al., 2014b] mentioned in the introduction section that, in the mesosphere and lower thermosphere, longer vertical wavelength components tend to contribute more to the MF than GW components with short vertical wavelength. However, since we are only able to calculate the MF at two levels, considering the uncertainty of the calculated MF results, it is very difficult to estimate the horizontal wind acceleration in this case, which depends upon the vertical gradient of the MF.

4. Model Simulations and Discussion

We note that the lidar and MTM observations resemble the GW packet's dispersion within the lower thermosphere as described in Heale et al., [2014a], where a spectrally broad GW packet was excited at lower altitude. Thus, this model is utilized here to demonstrate the dispersion process of the medium scale wave packet identified in this study. By using the experimentally observed temperature, horizontal wind and GW parameters, a numerical model simulation is constructed for a GW packet to investigate its vertical and horizontal variations in the mesopause region. The numerical model is a 2D nonlinear, fully compressible solution to the Euler equations, with Navier-Stokes viscosity [e.g., Snively et al., 2013] using an adaptation of the Clawpack finite volume routines [Leveque, 2004; Snively and Pasko, 2008, and references cited therein]. The Clawpack routines solve a hyperbolic system of equations by decomposing the fluxes between cell boundaries into a series of characteristic waves with characteristic speeds, which are then propagated at each time step. The main system of equations solve for conservation of mass, momentum, and energy which include gravity as a balanced source term via the f-wave method [Bale et al., 2002]. Dissipation is then accounted for via a time-split method that applies thermal conduction and molecular viscosity to the previously solved system of equations. Gravity waves are excited with a time-dependent vertical body forcing which acts as a source term to the system of equations [e.g., Heale et al., 2014a]. Finally, the solution is coupled with a nonlinear solution to airglow photochemistry and associated perturbations due to gravity wave dynamics [e.g., Snively, et al., 2010; Snively, 2013; references cited therein].

In this model simulation, the steady state background wind is specified to match the meridional wind observations from the nearby MWR. The model background temperature profile is constructed using a combination of an NRLMSISE-00 profile [Picone et al. 2002]

set to Bear Lake Observatory, and the nightly averaged Na lidar data. The lidar data is spliced into the MSIS profile over the 80-105km altitude range and smoothed. The later discussed reverse ray-trace, used to determine the horizontal propagation distance between the tropopause and 50km, utilizes this MSIS background temperature structure to determine the wave refraction. The temperature background, between 80 and105km, is set to be constant in time and match the Na lidar measured nightly averaged temperature profile (see Figure 5). The horizontal domain was specified to be 2800 km with 10-km resolution, and 300 km in the vertical (0.5 km resolution), with results output every 5-minutes. The GW was excited via a vertical body forcing centered at z_0=50 km, x_0=500 km. Note that x represents the meridional direction in this simulation, since the wave was propagating mostly in this direction, and z is altitude. The equation for the spectrally broad gravity wave source is given by:

$$F(x,z,t) = Bcos(k(x-x_0) - \omega(t-t_0))\exp\left[-0.5\left[\frac{(x-x_0)^2}{\sigma_x^2} + \frac{(z-z_0)^2}{\sigma_z^2} + \frac{(t-t_0)^2}{\sigma_t^2}\right]\right] \quad (4)$$

, where B is the amplitude, k = 2π/260km, ω = 2π/92min, t_0 = 368 minute, σ_x = 260 km, σ_z = 3 km, σ_t = 92 minutes. Here, the period and horizontal wavelength are set to match the MTM observations near OH layer at BLO and the GW packet propagates towards the north. The amplitude is chosen to be large enough to match the lidar observation, and this is also found sufficient to limit the nonlinear interactions and instability during the process near the observation region. Indeed, at further distances away ~1800 km from the source, the waves become strongly nonlinear as they achieve instability and breaking. In other words, energy and momentum deposition during wave dissipation are small enough near the observation site that the gravity wave-mean flow interaction does not dramatically affect background temperature and wind field, therefore the linear GW theory can still be applied approximately. It has to be noted that the simulation is to qualify the spatial and temporal

variations during the packet propagation process, and captures only part of the full spectrum of dynamics observed during the event. Due to the complex nature of this process, differences between model results and the observations are expected.

After running the simulations, we introduce two "virtual lidar" stations at horizontal positions of x = 950 km (LIDAR1) and x = 1800 km (LIDAR2) respectively in order to obtain a time series of the vertical GW variations in the mesopause region at single locations. The station at x=950 km is chosen to match the lidar observation the best, which is slightly less than 2 horizontal wavelength away from the source regions. As shown in the following discussion, LIDAR1 that is positioned 450 km away from the source will tend to "observe" the higher frequency (long vertical wavelength) components of the packet, which travel more vertically than horizontally. Whereas LIDAR 2 is 1300 km away from the source region and will "observe" the dominant lower frequency components (short vertical wavelength) of the packet, since the high frequency components have already propagated through the mesopause region and well into thermosphere. The simulation will later indicate these "observed" effects are caused by a combination of wave packet dispersion and wind filtering. In an attempt to locate the geophysical source of this wave packet, by using the same NRLMSISE-00 profile for background, a basic ray-trace analysis on a downward propagating wave, originating at the source altitude (50km), is conducted. The result suggests that the wave would propagate 730km horizontally (northward) before getting to the source altitude (z = 50 km) in the model simulation. Therefore a rough estimate of the total horizontal propagation distance from tropopause to MLT would be ~1180km (730 km + 450 km). Indeed, the NOAA NEXRAD reflectivity data, archived at website: http://gis.ncdc.noaa.gov/map/viewer/#app=cdo&cfg=radar&theme=radar&display=nexrad, reveal a strong storm system near the south side of Arizona-Mexico border, which is roughly 1200 km away from Logan, UT (Figure 6), during the early evening on September 1st (UT

day September 2nd) that lasted for more than 2 hours. Considering the horizontal distance between source location of this storm system in the troposphere and its site of penetration in the tropopause, the ray-tracing technique reasonably locates the source of the GW packet. It is important to note, however, that the model source of the simulated wave at 50 km, and its chosen spatial and temporal characteristics, are only an approximation of a packet that may have originated from a tropospheric source at relatively greater distances.

Figure 7 shows the time-series of the temperature perturbation that LIDAR1 would observe in the model simulation, along with the Na lidar measured temperature perturbations during that night. Here, using a high pass filter, the lidar temperature perturbation is derived by removing the modulations with period longer than 3-hour. It has to be pointed out that the starting time of this model run is arbitrary, thus, the time shift of the GW features in the simulations when compared to the lidar temperature observations, are not critical. As the figure shows, these simulated GW packet perturbation closely resembles the actual Na lidar measured temperature variations and indicates the characteristic descending GW shape with the decreasing vertical wavelength. In this figure, at early time, LIDAR1 observes the high frequency (1-hour) portion of the wave packet that propagates with the largest vertical group velocity and vertical wavelength. Compared with the simulation, the less vertical wavelength in the lidar data below 90 km is most likely due to the much larger horizontal wind variations in reality.

More recent research [Eckermann 1997, Sartelet et al. 2003, Vanderhoff et al. 2008, Senf and Achatz 2011, Huang et al. 2013, Heale and Snively, 2015] has suggested that the time-dependence of the background wind plays an important role in gravity wave propagation. The changing background wind will act to alter the ground relative frequency of the gravity wave. This can lead to a reduction in both reflection and critical level filtering,

while increasing upward transmission. Due to the time dependence of the background wind, the critical level becomes transient at a given location and will change location with the phase of the wind; therefore there is less time for a wave and critical level to "interact" at a given altitude. Also, the changing background wind tends to change the ground relative frequency such that a 'hard' critical level does not occur. However, under simplifying assumptions of hydrostatic and slowly varying motion, inferred from linear and inviscid steady-state wave structure, the changes of mean wind can alter the structure of the GW packet near the critical level as defined by [Booker and Bretherton, 1967]

$$m^2 \sim \frac{N^2}{(U_h - c)^2} \qquad (5)$$

In this case, the strong southward wind during early part of the night (see Figure 8) will turn this portion of the spectrum to even larger vertical wavelength by increasing the denominator in Eq. 5 and vertical group velocities due to Doppler shift, resembling the lidar observations in Figure 4. At later time, the simulated temperature perturbation shows the parts of the packet, which have shorter vertical wavelength and smaller vertical group velocities, but the modulations are limited below roughly 90 km, which is also extremely similar to the lidar temperature observations. The wind in the GW propagating direction (meridional direction) is later turning northward (see Figure 8) and, thus, shifts the packet to even shorter vertical wavelength by decreasing the denominator in Eq.5. During this time period, the temperature perturbation simulation shows that, at lower altitudes in the mesopause region, the perturbations are dominated by low frequency component, while the amplitudes of high frequency component become fairly weak. In Figure 7, the simulation also reveals a considerable temperature enhancement structure above 100 km during the second half of the night that was not evident in the lidar measurement. The model results suggest this is likely related to horizontal expansion of some secondary effect when wave instability occurs during

the second half the night near 100 km altitude around x=1600 km. Indeed, in a similar model run with much smaller forcing amplitude, this temperature enhancement structure does not emerge at this location. As expected, the horizontal wind plays significant role in this simulated GW packet dissipation process when approaching its critical level. Towards the end of the simulation, the wind possesses a strong enough positive amplitude that it acts to critical level filter the susceptible portion of the packet. Therefore, these two effects in tandem cause the appearance of the descending pattern and the decreasing vertical wavelength in time.

Figure 8 shows that the simulated variations of horizontal wind component in the wave propagation direction (primarily meridional) generally agree with those of the lidar measured meridional wind in high spatial and temporal resolutions. However, when comparing the lidar measurement with that in the simulation, it is found that the lidar measured meridional wind experienced some large perturbations once the vertical wavelength became shorter after UT 09:00 below 89 km, which are not captured in the simulated wind and do not appear as a result of the evolving medium scale waves. The large perturbation may be interpreted by the simplified relationship between horizontal wind perturbation and vertical wavenumber, $u_h' \propto m^{1/2}$, near the critical level [Booker and Bretherton, 1967]. Here, u_h' represents the gravity wave induced horizontal wind perturbation along the wave propagating direction. Therefore, the aforementioned increase of vertical wavenumber, *m*, is able to induce large wind perturbation in the meridional direction in this region when the waves are approaching the critical level, which occurred around 10:00 UT near 87 km as mentioned before. The absence of this feature within the simulation could be due to other wave dynamics that were present during the event. The model simulation also tries to enforce a specified model wind field, thus limiting wave-background interactions. The specified model wind is much smoother than reality, underestimating the extremely dramatic swing of

meridional wind in the lidar observation during the first half of the night when the meridional wind reversed from close 200 m/s southward to several tens of m/s northward within a couple of hours. Such huge reverse of horizontal wind in such short time span implies a sharp transition of over 100 m/s amplitude that is not understood as this point. It may suggest very strong tidal and larger scale wave activity, or impacts of stronger, faster waves present at earlier times that are not simulated. It is worth noting that gravity wave deposition of momentum and self-acceleration could also alter the spatial and temporal structure of the packet, and tend to increase the vertical wavelength and facilitate the packet to penetrate the critical level [Fritts and Dunkerton, 1984; Fritts et al., 2015]. However, the fact that neither strong, lasting impacts on flow, nor evidence of the increasing vertical wavelength were observed by the Na lidar that night implies the absence of this scenario during this night. The model results also suggest insufficient amplitudes to achieve strong self-acceleration for the simulated spectrum under the specified conditions.

If the lidar were observing the same GW packet propagation at a location further away from the simulated source region, a completely different scenario would be "observed". Figure 9 shows the same GW packet induced temperature perturbation "observed" by LIDAR2, 1300 km away from the source region. In this case, the portion of the packet that LIDAR2 "observes" is much more spectrally uniform in time (quasi-monochromatic) with much larger amplitude (more than doubled) than those "observed" at LIDAR1. Contrary to the scenario above LIDAR1, the packet is not subject to critical level filtering by the background wind due to its higher horizontal phase velocity and, thus, dominates the second half of the night. The simulated wave shows signs of breaking/instability at the LIDAR 2 location, due to its relatively large amplitude. The simulation suggests that, while the model results do not show wave breaking at LIDAR1, breaking could occur downstream of this site (further north), where the central frequency of the wave packet dominates and the amplitude

of the wave becomes larger. There is also slightly altitude dependence in the vertical wavelength however, due to the Doppler shifting of the gravity wave by the background wind. Note that, although this scenario does not match well with the lidar data for this event, these simulated results are similar to most of the GW events discussed in the other literatures and publications from ground-based measurements. This suggests that, for the same GW packet, the location of the lidar or any other instruments relative to the source region will determine what GW characteristic can be observed. In other words, to have a comprehensive view of the GW packet dissipation and propagation, simultaneous observations from a few ground-based instruments spacing properly in horizontal direction would be needed.

The numerical model also simulates gravity wave perturbations to OH layer and associated OH band emissions [e.g., Snively, et al., 2010; Snively, 2013; references cited therein], along with density perturbations to the mesospheric Na layer. Figure 10 shows the North-South sliced Keogram of the model's simulated OH (6-2) band brightness-weighted temperature perturbations, which arise near 87 km at x=950 km (top). They are compared with BLO MTM rotational temperature observation for the same arrangement (bottom). The two agree remarkably well, although dynamics are necessarily simpler in the model simulation due to the nature of the specified source and background. Note that the data may suggest some form of instability/breaking after ~8 UT as a result of the wave being shifted to smaller vertical wavelength by the background wind. This may help explain the transition from longer to shorter periods seen in the wavelet data at z=87km in Figure 2.

5. Conclusion

While most reports of GW events observed via ground-based instruments have focused on quasi-monochromatic wave propagation, the Na lidar at Utah State University has captured evidence of a dispersing GW spectrum in the mesopause region. This event occurred

on the night of September 2nd, 2011, and the lidar data are supported by additional observations from a suite of instruments at nearby Bear Lake Observatory. The temperature perturbations were found to be dominated by GW components with relatively long vertical wavelength and higher frequencies at high altitudes during the early part of the night, while components with shorter vertical wavelength and lower frequencies were considerably stronger at lower altitude and during the second half of the night. The MTM's observations near OH layer (~87 km) and O_2 layer (94 km) confirm the Na lidar observation by measuring the perturbation periods of 92-minute and 75-minute near these two layers, respectively. Such a smooth frequency evolution of GW components is rarely seen in experimental studies. The calculated vertical group velocity suggests that, near both nightglow levels, the wave was slowing down in the vertical direction with increasing vertical wavenumber, implying refraction of the wave occurring during the second half of the night as it approaches a critical level. At the same time, the momentum flux calculations near the two nightglow layers indicate the significant flux occurred during the first half of the night when the mesopause region was dominated by GW components with longer vertical wavelength.

The remarkable similarities between this observation and model predictions of selective dispersion and dissipation of spectrally-broad GW packets motivated a specific numerical case study for this GW event, based upon observations by Na lidar, MTM and MWR. After the packet is forced at upper stratosphere, it has propagated vertical and horizontally in the model, where two "virtual" lidar stations are set up 450 km and 1300 km away from the source region to "observe" the temperature perturbations in the mesopause region. The simulation shows that the station close to the source region would observe an extremely similar scenario to the Na lidar observations on the night of September 2nd, 2011, while at the station that is farther away, completely different features would be measured (quasi-monochromatic modulation dominated by low frequency GW components with short

vertical wavelength). This is because, within the packet spectrum, the high frequency components with long vertical wavelength propagate more vertically than horizontally and, thus, reach the mesopause region earlier and are confined to a horizontal range that is relatively close to the source, while the low frequency components with short vertical wavelength behave in the opposite manner. The horizontal wind is found to play highly important role in this process by generating a critical level for the high frequency packet components during the second half of the night, modulating the vertical wavelength and preventing them from reaching higher altitudes, which can be clearly seen in both the lidar observation model simulations.

The model also successfully reproduces primary features of the MTM's OH layer observations, although species density variations are calculated only for the ~1 hour wave dynamics of interest and are thus less complicated by additional dynamics those seen under actual MLT conditions. The model simulation is conducted under constant (in time) background temperature and smoothed background wind, and does not incorporate comprehensive tidal dynamics beyond an approximate description of the evolving winds. This also limits the nonlinear wave-mean flow interaction, although it provides insight into the observable features of the gravity event, i.e., its refraction, dispersion, dissipation, and modulation to the airglow and species layers. These limitations cause some discrepancies between the model results and lidar observations, such as the wave instability induced considerable temperature enhancement near 100 km that did not appear in the lidar temperature, along with absence of enhanced wind perturbation near critical level in the simulation.

Nonetheless, with the assistance from the numerical model, we can conclude that the lidar observed temperature perturbation "anomaly" belongs to an important phase during the

dispersion of a spectrally broad GW packet that was excited relatively close the Na lidar station at northern Utah. A basic ray-trace analysis on a downward propagating wave, couple with NOAA NEXRAD observation, suggests that the lidar observed wave packet could be excited by a strong storm system ~1200 km south of USU during early evening of September 1st near the Mexico side of Arizona-Mexico border. Observing this process in the mesopause region above northern Utah, the dominant observable GW components were shifting from high frequency components with large vertical wavelength to lower frequency component with shorter vertical wavelength. Near USU, the collaborative observations conducted by a suite of instruments provided a detailed view of this process, helping to understand a key phase of the complex GW packet propagation, dispersion, and dissipation process. However, since ground-based instrument observations are highly sensitive to the altitudes of observation and the horizontal distances relative to the source region, to have a complete view of the GW dispersion and dissipation processes, several ground-based observations would need to be made along the GW propagating direction with proper spacing in the horizontal domain. These observations underscore the need for (and value of) multiple instrument observations in addition to synergistic modeling for the interpretation of wave processes that occur over hundreds-to-thousands of kilometer spans.

Acknowledgement:

This study was performed as part of a collaborative research program supported under the Consortium of Resonance and Rayleigh Lidars (CRRL), National Science Foundation grants (NSF) AGS-1135882. Bear Lake Observatory instrument operations are supported in part by NSF Collaborative Research grants 1042227 and 1452744. The lidar data of this study are available at the CRRL Madrigal data base at: http://madrigal.physics.colostate.edu/htdocs/. The SkiYMet MWR was operated at BLO in

collaboration with Prof. N.J. Mitchell at The University of Bath, U.K., under a Natural Environment Research Council grant NE/H009760/1. The model simulation work was supported under NSF grant AGS-1151746 to Embry-Riddle Aeronautical University.

Reference:

Acott, P. E., C. Y. She, D. A. Krueger, Z. Yan, T. Yuan, J. Yue, S. Harrell (2011), "Observed nocturnal gravity wave variances and zonal momentum flux in midlatitude mesopause region over Fort Collins, Colorado", J. Atmos. Solar-Terr. Phys.73,449-456.

Alexander, M. J., J. C. Gille, C. Cavanaugh, M. Coffey, C. Craig, V. Dean, T. Eden, G. Francis, C. Halvorson, T. Hannigan, R. Khosravi, D. Kinneson, H. Lee, S. Massie, N. Nardi, and A. Lambert (2008), Global estimates of gravity wave momentum flux from High Resolution Dynamics Limb Sounder (HIRDLS) observations, J. Geophys. Res., 113, D15S18, doi:10.1029/2007JD008807.

Alexander, M. J. and Holton, J. R. (2004): On the spectrum of vertically propagating gravity waves generated by a transient heat source, Atmos. Chem. Phys., 4, 923-932, doi:10.5194/acp-4-923-2004.

Bale, D., R. J. LeVeque, S. Mitran, *and* J. A. Rossmanith *(*2002*),* A wave-propagation method for conservation laws and balance laws with spatially varying flux functions, SIAM J. Sci. Comput., 24, 955–978.

Booker, J. P. and F. P. Bretherton (1967), The critical layer for internal gravity wave in a shear flow. J. Fluid Mech., 27, 513-539.

Cai, X., T. Yuan, Y. Zhao, P.-D. Pautet, M. J. Taylor, *and* W. R. Pendleton Jr *(*2014*),* A coordinated investigation of the gravity wave breaking and the associated dynamical instability by a Na lidar and an Advanced Mesosphere Temperature Mapper over Logan, UT

(41.7°N, 111.8°W), J. Geophys. Res. Space Physics, 119, 6852–6864, *doi:*10.1002/2014JA020131.

Chen, C., X. Chu, A. J. McDonald, S. L. Vadas, Z. Yu, W. Fong and X. Lu (2013), Inertia-gravity waves in Antarctica: A case study using simultaneous lidar and radar measurements at McMurdo/Scott Base (77.8_S, 166.7_E), J. Geophys. Res. Atmos., 118, 2794–2808, doi:10.1002/jgrd.50318.

Eckermann, S. D. (1997), Influence of wave propagation on the Doppler spreading of atmospheric gravity waves, J. Atmos. Sci., 54, 2554 – 2573

Ern, M., P. Preusse, M. J. Alexander, and C. D. Warner (2004), Absolute values of gravity wave momentum flux derived from satellite data, J. Geophys. Res., 109, D20103, doi:10.1029/2004JD004752.

Fritts, D. C., P-D. Pautet, K. Bossert, M. J. Taylor, B. P. Williams, H. Limura, T. Yuan, N. J. Mitchell and G. Stöber (2014a), Quantifying Gravity Wave Momentum Flues with Mesosphere Temperature Mappers and Correlative Instrumentation, J. Geophys. Res. Atmosphere, 119, DOI: 10.1002/2014JD022150.

Fritts, David C., Kam Wan, Joseph Werne, Thomas Lund, and James H. Hecht (2014b), Modeling the implications of Kelvin-Helmholtz instability dynamics for airglow observations, J. Geophys. Res. Atmospheres 119, no. 14: 8858-8871.

Fritts, D. C. and Vadas, S. L. (2008), Gravity wave penetration into the thermosphere: sensitiveity to solar cycle variations and mean wind, Ann. Geophys. 26: 3841-3861.

Fritts, D. and M. J. Alexander (2003), Gravity wave dynamics and effects in the middle atmosphere, Rev. Geophys., 41(1), 1003, doi:10.1029/2001RG000106.

Fritts, D. and T. J. Dunkerton (1984), A quasi-linear study of gravity-wave saturation and self-acceleration, J. Atmos. Scien. Vol. 41, No. 22, 3272-3289.

Fritts, D. C., B. Laughman, T. S. Lund, and J. B. Snively (2015), Self-acceleration and instability of gravity wave packets: 1. Effects of temporal localization, J. Geophys. Res. Atmos., 120, doi:10.1002/2015JD023363.

Heale, C. J., and J. B. Snively (2015), Gravity wave propagation through a vertically and horizontally inhomogeneous background wind, *J. Geophys. Res. Atmos., 120,* 1–20, doi:10.1002/2015JD023505.

Heale, C. J., J. B. Snively, M. P. Hickey, *and* C. J. Ali *(*2014a*),* Thermospheric dissipation of upward propagating gravity wave packets, J. Geophys. Res. Space Physics, 119, 3857–3872 *doi:*10.1002/2013JA019387.

Heale, C. J., J. B. Snively, and M. P. Hickey (2014b), Numerical simulation of the long range propagation of gravity wave packets at high latitudes, J. Geophys. Res., 119, 1–19.

Hines, C. (1960), Internal atmospheric gravity waves at ionospheric heights, Can. J. Phys., 38, 1441–1481.

Hocking, W. K., B. Fuller and B. Vandepeer (2001), Real-time determination of meteor-related parameters utilizing modern digital technology, , J. Atmo. Solar-Terr. Phys. 63, 155-169.

Huang, C. M., S. D. Zhang, F. Yi, K. M. Huang, Y. H. Zhang, Q. Gan, and Y. Gong (2013), Frequency variations of gravity waves interacting with a time-varying tide, Ann. Geophys., 31, 1731–1743, doi:10.5194/angeo-31-1731-2013.

Liu, X., J. Xu, J. Yue, and S. L. Vadas (2013), Numerical modeling study of the momentum deposition of small amplitude gravity waves in the thermosphere, Ann. Geophys., 31, 1–14.

LeVeque, R. J., and M. J. Berger (2004), Clawpack software version 4.6. www.clawpack.org.

Li, F., G. R. Swenson, A. Z. Liu, M. Taylor, and Y. Zhao (2007a), Investigation of a 'wall'wave event, J. Geophys. Res., 112, D04104, doi:10.1029/2006JD007213.

Li, T., C.-Y. She, H.-L. Liu, T. Leblanc, and I. S. McDermid (2007b), Sodium lidar–observed strong inertia-gravity wave activities in the mesopause region over Fort Collins, Colorado (41N, 105W), J. Geophys. Res., 112, D22104, doi:10.1029/2007JD008681.

Lu, X., A. Z. Liu, G. R. Swenson, T. Li, T. Leblanc, and I. S. McDermid (2009), Gravity wave propagation and dissipation from the stratosphere to the lower thermosphere J. Geophys. Res., 114, D11101, doi:10.1029/2008JD010112.

Meriwether, J. W. *(*1984*),* Ground based measurements of mesospheric temperatures by optical means*,* MAP Handb.*,* 13*,* 1–18*.*

Pautet, P.-D. M. J. Talor, W. R. Pendleton, Jr. Y. Zhao, T. Yuan, R. Esplin, and D. McLain (2014), Advanced mesospheric temperature mapper for high-latitude airglow studies, Applied Optics Vol. 53, Iss. 26, pp. 5934–5943.

Pendleton, W. R.Jr.*,* M. J. Taylor*, and* L. C. Gardner *(*2000*),* Terdiurnal oscillations in OH Meinel rotational temperatures for fall conditions at northern midlatitude sites*,* Geophys. Res. Lett.*,* 27*(*12*),* 1799–1802*.*

Picone, J. M., A. E. Hedin, D. P. Drob, and A. Aikin (2002), NRL-MSISE-00 empirical model of the atmosphere: Statisical comparisons and scientific issues, J. Geophys. Res., 107(A12), 1468, doi:10.1029/2002JA009430.

Sartelet, K. N. (2003), Wave propagation inside an inertial wave. Part I: Role of time dependence and scale separation, J. Atmos. Sci., 60, 1433 – 1447

Senf, F., and U. Achatz (2011), On the impact of middle-atmosphere thermal tides on the propagation and dissipation of gravity waves, J. Geophys. Res., 116, D24110, doi:10.1029/2011JD015794.

She, C. Y., T. Li, B. P. Williams, T. Yuan, and R. H. Picard (2004), Concurrent OH imager and sodium temperature/wind lidar observation of a mesopause region undular bore event over Fort Collins/Platteville, CO, J. Geophys. Res., 109, D22107.

She, C. Y., J. Sherman, T. Yuan, B. P. Williams, K. Arnold, T. D. Kawahara, T. Li, L. F. Xu, J. D. Vance, P. Acott and D. A. Krueger (2003), The first 80-hour continuous lidar campaign for simultaneous observation of mesopause region temperature and wind, Geophys. Res. Lett. 30, 10.1029/2002GL016412.

Snively, J. B., K. Nielsen, M. P. Hickey, C. J. Heale, M. Talyor, and T. Moffat-Griffin, Numerical and statistical evidence for long-range ducted gravity wave propagation over Halley, Antarctica, Geophys. Res. lett., 40 (18), 4813–4817, 2013.

Snively, J. B., and V. P. Pasko (2008), Excitation of ducted gravity waves in the lower thermosphere by tropospheric sources, J. Geophys. Res., 113, A06303, doi:10.1029/2007JA012693.

Snively, J. B. (2013), Mesospheric hydroxyl airglow signatures of acoustic and gravity waves generated by transient tropospheric forcing, Geophys. Res. Lett., 40, 4533–4537, *doi:*10.1002/grl.50886.

Snively, J. B., V. P. Pasko, and M. J. Taylor (2010), OH and OI airglow layer modulation by ducted short-period gravity waves: Effects of trapping altitude, *J. Geophys. Res.*, 115, A11311, doi:10.1029/2009JA015236.

Taylor, M. J., L. C. Gardner, *and* W. R. Pendleton Jr. *(*2001*),* Long period wave signatures in mesospheric OH Meinel (6,2) band intensity and rotational temperature at midlatitudes, Adv. Space Res., 27*(*6–7*),* 1171–1179.

Vadas, S. L., and D. C. Fritts (2005), Thermospheric responses to gravity waves: Influences of increasing viscosity and thermal diffusivity, J. Geophys. Res., 110, D15103, doi:10.1029/2004JD005574.

Vanderhoff, J. C., K. K. Nomura, J. W. Rottman, and C. Macaskill (2008), Doppler spreading of internal gravity waves by an inertia-wave packet, J. Geophys. Res., 113, C05018, doi:10.1029/2007JC004390.

Walterscheid, R., G. Schubert, and D. Brinkman (2001), Small-scale gravity waves in the upper mesosphere and lower thermosphere generated by deep tropical convection, J. Geophys. Res., 106(D23), 31,825–31,832.

Yu, Y., M. Hickey, and Y. Liu (2009), A numerical model characterizing internal gravity wave propagation into the upper atmosphere, Adv. Space Res., 44(7), 836–846.

Yuan, T., P.-D. Pautet, Y. Zhao, X. Cai, N. R. Criddle, M. J. Taylor and W.R. Pendleton, Jr. (2014), Coordinated investigation of mid-latitude upper mesospheric temperature inversion layers and the associated gravity wave forcing by Na lidar and Advanced Mesospheric Temperature Mapper in Logan, Utah, J. Geophys. Res. Atmos., 119, doi:10.1002/2013JD020586.

Yuan, T., H. Schmidt, C. Y. She, D. A. Krueger, and S. Reising (2008), Seasonal variations of semidiurnal tidal perturbations in mesopause region temperature and zonal and meridional winds above Fort Collins, Colorado (40.6°N, 105.1°W), J. Geophys. Res., 113, D20103, doi:10.1029/2007JD009687.

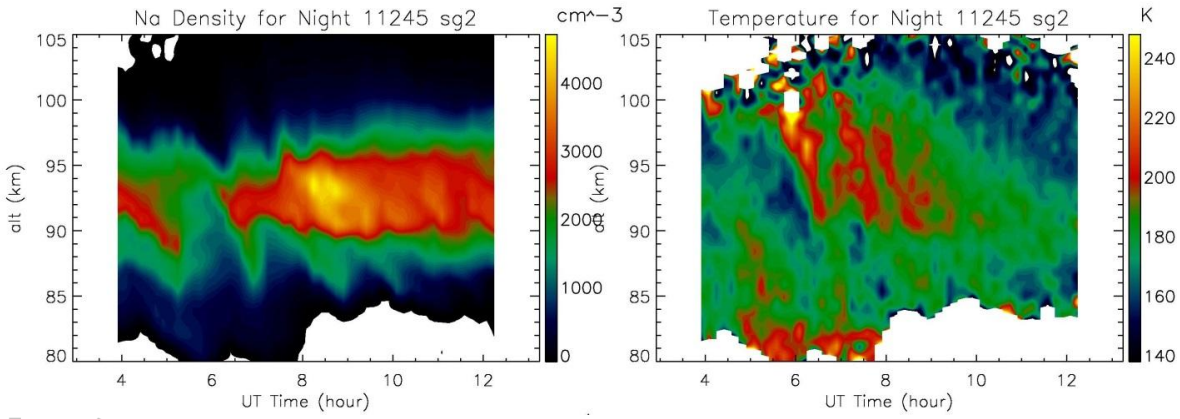

Figure 1. The USU Na lidar observed mesospheric Na layer (left) and temperature variations on September 2nd, 2011. The lidar data are processed with 1 km and 10-minute spatial and temporal resolutions.

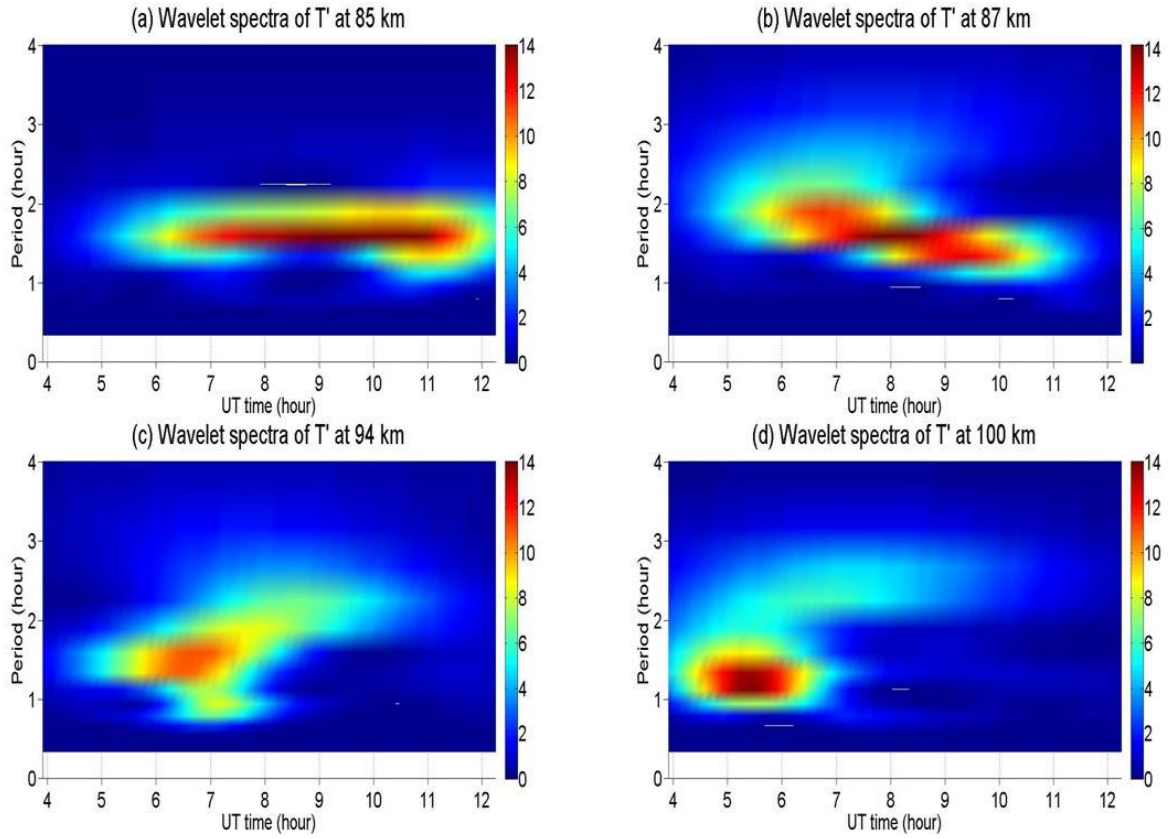

Figure 2. The wavelet analysis results at 85 km (top left), 87 km (top right), 94 km (bottom left) and 100 km (bottom right). The analysis is applied on the Na lidar temperature measurements that are band pass filtered to remove the modulations with period longer than 3-hour and those with period shorter than 50-minute.

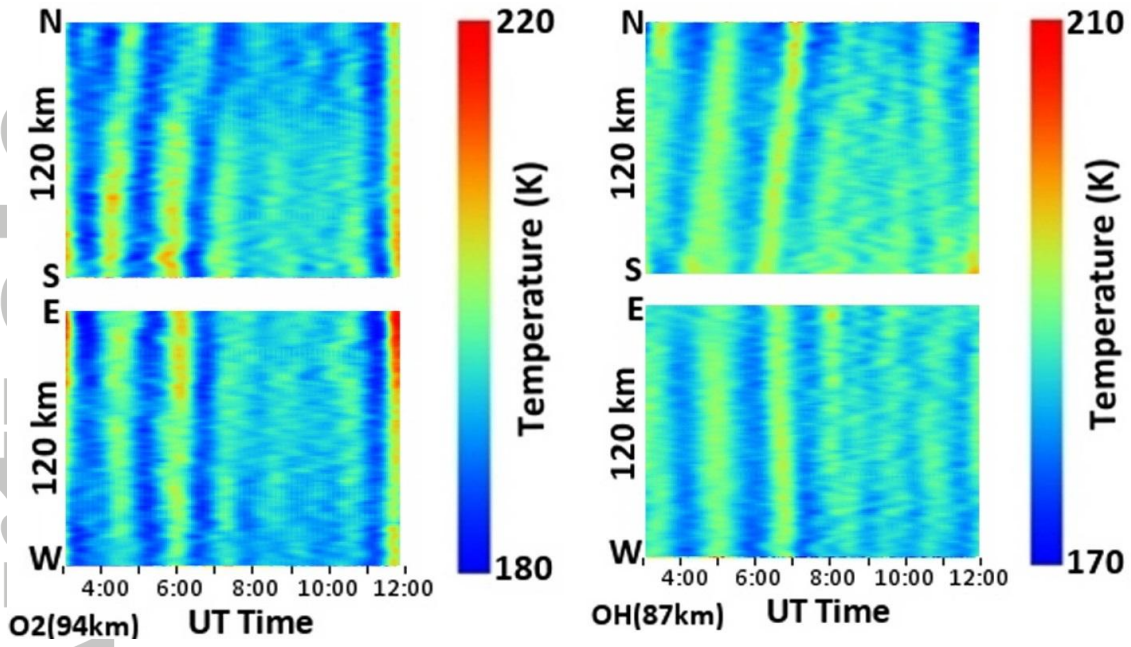

Figure 3. The North-South (top row) and East-West (bottom row) Keograms of MTM temperature measurements near O_2 layer (left column) and OH layer (right column) observed at Bear Lake Observatory on September 2nd, 2011.

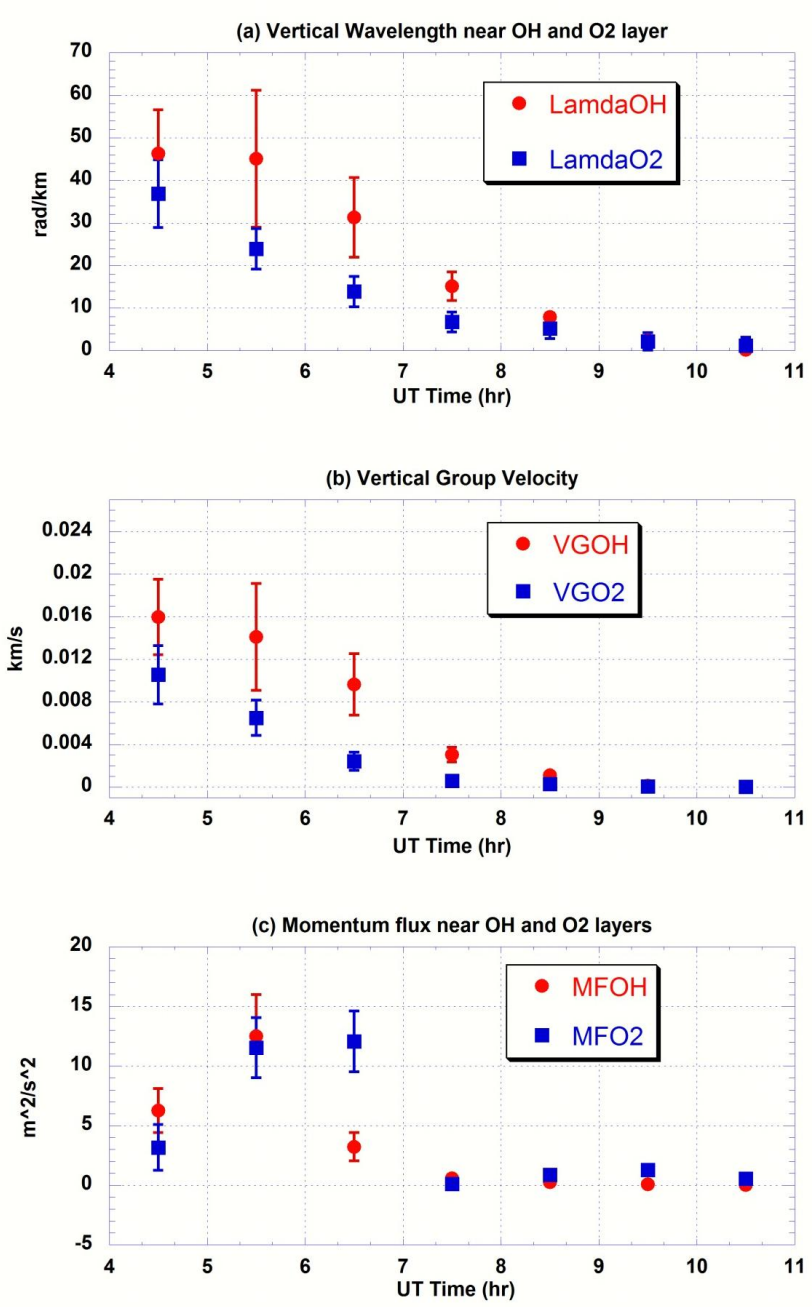

Figure 4. The variations of the absolute value of vertical wavelength of the GW packet (top) near O_2 layer (squres) and OH layer (solid dots); the GW packet's vertical group velocities (middle) near O_2 layer and OH layer; the momentum flux variations (bottom) near the two nightglow levels.

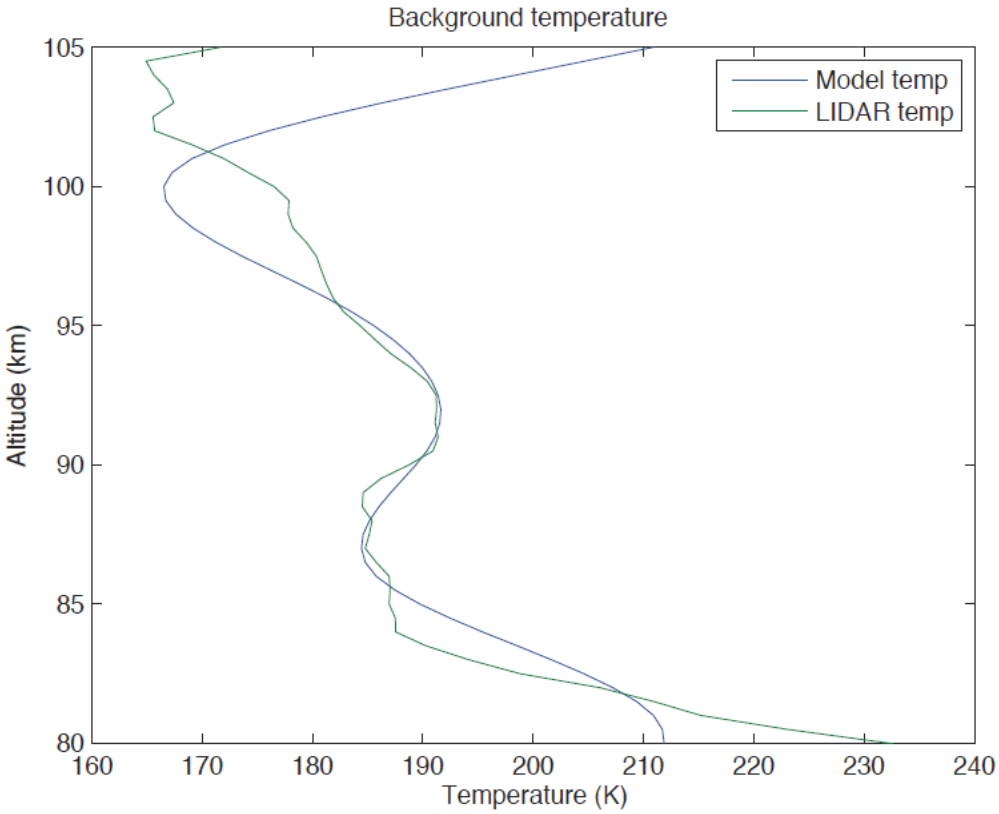

Figure 5. The comparison of the lidar measured nightly averaged temperature and the constant background temperature applied in the model simulation.

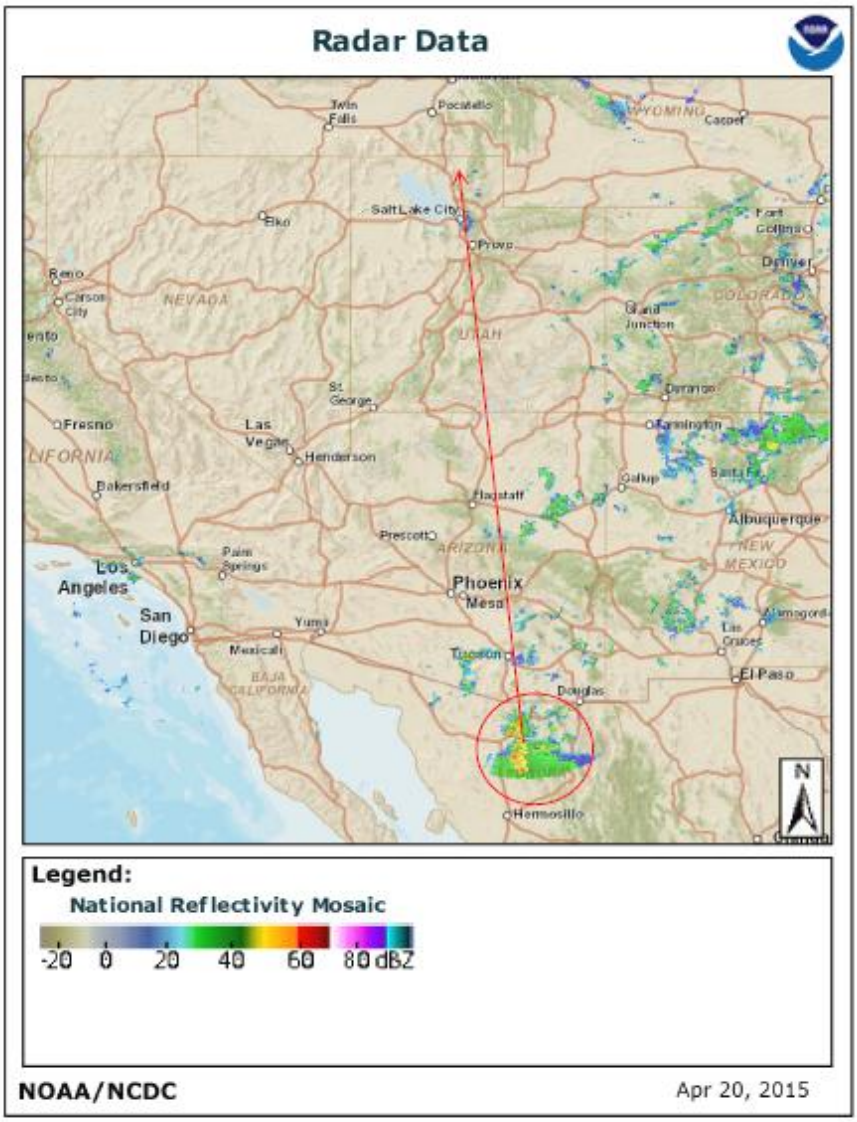

Figure 6. National NEXRAD reflectivity at 09:30 pm local time on September 1, which is UT 03:30 on September 2nd, over the southeast climate region of United States. The red circle marks an active storm system, ~1200 km south of the USU Na lidar station, which is likely the source for the lidar observed GW packet.

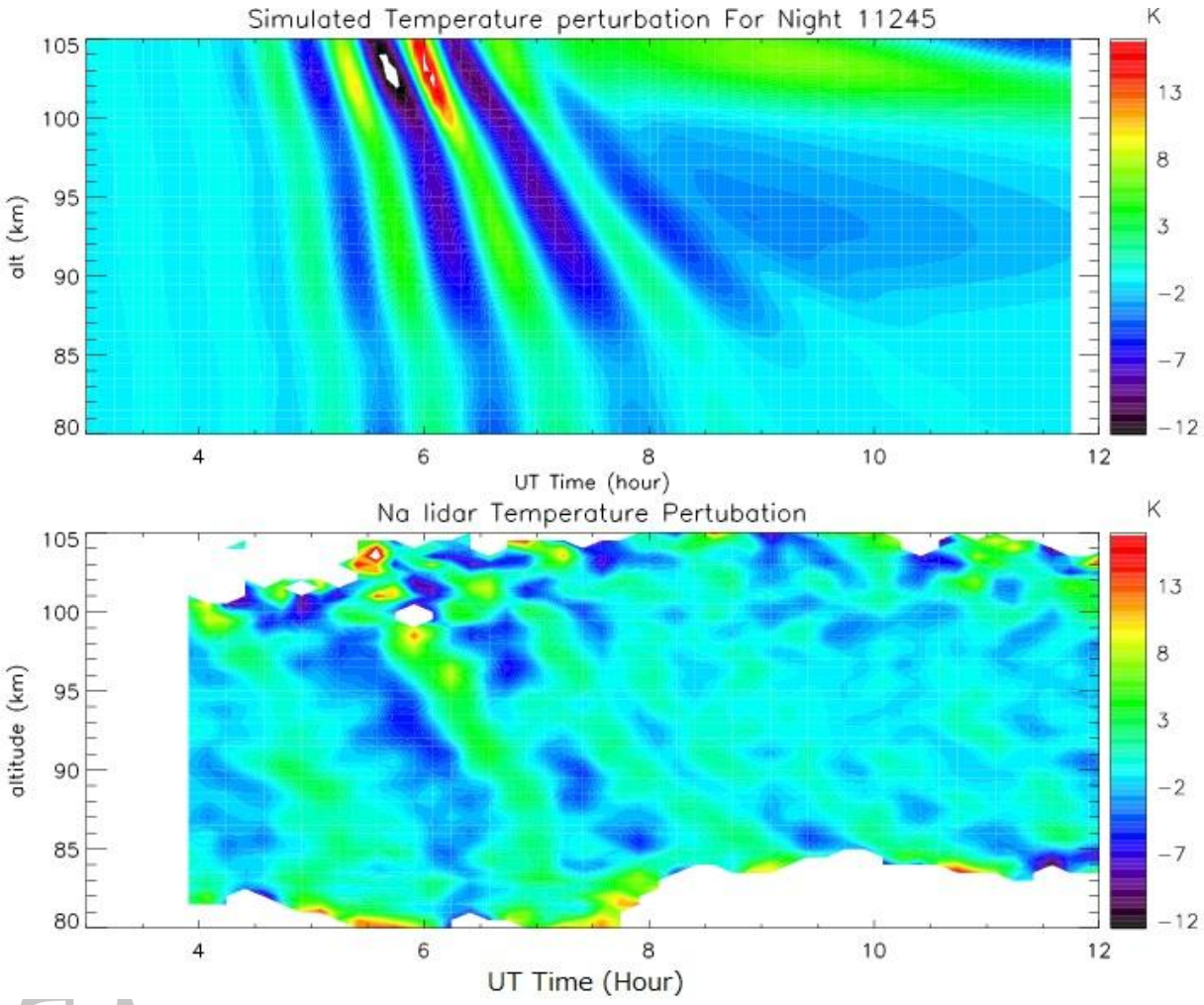

Figure 7. The simulated temperature perturbations in the mesopause region above the virtual station LIDAR1 x=950 km (top) and the Na lidar temperature perturbation measurements (bottom) on night of September, 2nd, 2011. The plots are aligned accordingly to the UT time.

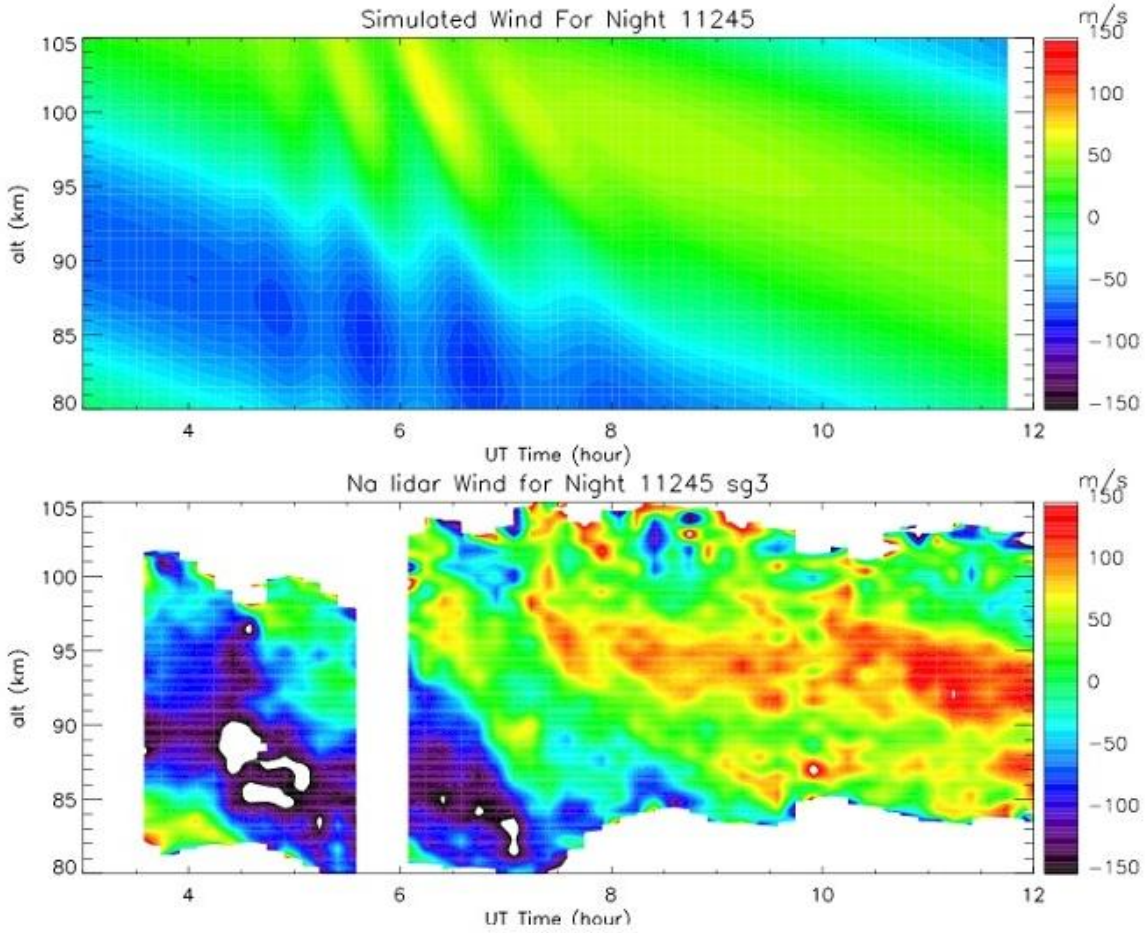

Figure 8. The comparison of the model simulated horizontal wind variations above the virtual station LIDAR1 x=950 km (top) in the GW propagating direction (mostly in meridional direction) and the Na lidar measured meridional wind (bottom) on night of September, 2nd, 2011. The plots are aligned accordingly to the UT time. The white areas between 84 km and 90 km from ~UT 4.5 to ~UT 5.0 in lidar measurements are due to outside the color bar.

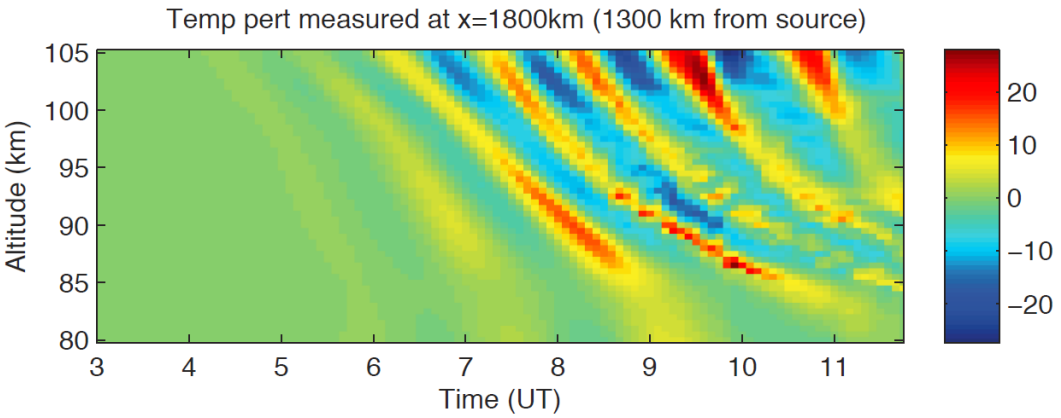

Figure 9. The simulated temperature perturbation of the GW packet within the mesopause region above the virtual station LIDAR2 x=1800 km.

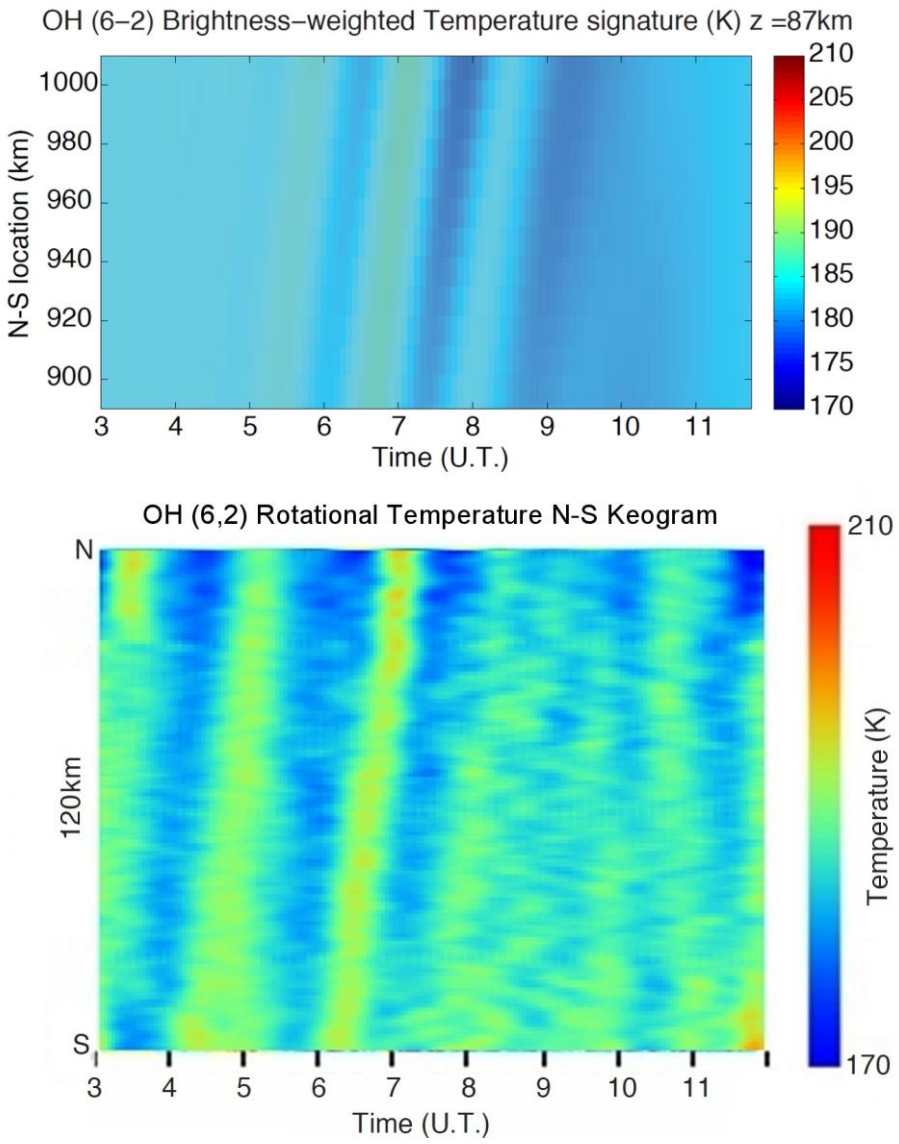

Figure 10. The comparison between the MTM OH temperature observations and the module simulated OH (6-2) band temperature modulations by the same GW packet.